Kirigami Oscillators: Nonlinear Free and Forced Responses

Francesco Danzi
University of California, Merced
Hongcheng Taoh
Purdue University West Lafayette
Christian Silva
Purdue University West Lafayette
James Gibert
`jgibert@purdue.edu`

Purdue University West Lafayette

Research Article

Keywords: Kirigami, Helmholtz-Duffng Oscillator, Nonlinear Oscillator, Quasi-mechanisms, Free and Forced Oscillation, Nonlinear Damping

Posted Date: October 30th, 2024

DOI: https://doi.org/10.21203/rs.3.rs-5283451/v1

Additional Declarations: No competing interests reported.

Kirigami Oscillators: Nonlinear Free and Forced Responses

Francesco Danzi[1,2] · **Hongcheng Tao**[2] · **Christian E. Silva** [2,3] · **James M. Gibert**[2]

Received: date / Accepted: date

Abstract Inspired by the ancient Japanese art of kirigami, slitted plastic sheets, termed kirigami springs, were designed, fabricated, and characterized, utilizing the quasi-mechanism behavior of various slit patterns. Quasi-static tension tests determined the spring stiffness, and experimental transient responses were analyzed to infer system damping. A system of two parallel-connected kirigami springs, attached to a mass oscillating on a smooth track, was modeled as a 1 DOF Helmholtz-Duffing oscillator with nonlinear damping. The system's free and forced responses were compared to experimental and numerical results using asymptotically valid solutions derived via the Method of Multiple Time Scales. This approach provides an unprecedented degree of programmability in the constitutive relations for nonlinear oscillators and is straightforward to implement.

This project was financially supported through the Purdue Research Foundation and the NSF CAREER Award: CMMI 2145803.

F. Danzi
E-mail: fdanzi@ucmerced.edu

H. Tao
E-mail: taoh@purdue.edu

C.E. Silva
E-mail: cesilva@purdue.edu

J. M. Gibert (Corresponding Author)
E-mail: jgibert@purdue.edu

[1] Department of Mechanical Engineering, University of California, Merced
[2] School of Mechanical Engineering, Purdue University
[3] Facultad de Ingeniería en Mecánica y Ciencias de la Producción, Escuela Superior Politécnica del Litoral, ESPOL, Km 30.5 Vía Perimetral, Guayaquil Ecuador

Keywords Kirigami · Helmholtz-Duffing Oscillator · Nonlinear Oscillator · Quasi-mechanisms · Free and Forced Oscillation · Nonlinear Damping

1 Introduction

Originally developed for decorative purposes, Origami and Kirigami are ancient Japanese arts that exploit folding and cutting to create a 3D complex geometry from a 2D flat sheet of paper. These art forms have evolved into valuable tools in the scientific and engineering fields, providing creative solutions to complex problems through the principles of folding and cutting. However, while Origami has been widely used to inspire the design of new engineering structures and materials [1–3], Kirigami has only recently been exploited by the engineering community for applications ranging from grasping robots [4, 5], programmable shapes [6–8], crawling robots [9], morphable structures [10, 11], solar trackers [12], actuators and sensors [13, 14], and metamaterials [15–20]. To the authors' knowledge, the use of Kirigami in vibration applications is largely unexplored and is currently prominent; examples are studies characterizing the modal properties of Kirigami structures [21, 22], flexural wave control [23], and pressure sensing via a resonant circuit [24].

The purpose of this study is to characterize the properties of slitted membranes, henceforth dubbed kirigami springs, through the use of static and dynamic tests. The proposed springs provide a straightforward method for tuning the stiffness of a system and may be used to design novel nonlinear oscillators. Herein we did not attempt to derive an analytical model that relates the topology of the cuts to the apparent mechanical response; we rather focused on the observed global mechanical response arising from quasi-static tests. The reader interested in the former aspect is directed to the scientific literature that aims to address these nuances [25–30].

The remainder of the paper is organized as follows. In Section 2, we provide a simple yet compelling motivation for the exploitation of Kirigami patterns as a means to tune nonlinear constitutive relations. We further discuss the pattern selected in Section 2.1. The method we used to fabricate the springs is detailed in Section 3.1. Section 3.2 details the quasi-static tests performed to determine the stiffness coefficients. In Section 3.3, we describe the transient tests and elucidate the procedure used to extrapolate the damping coefficients. In Section 4, we analyze the forced response of the system and compare the experimental time responses against the asymptotically valid solutions obtained via the Method of Multiple Time Scales.

2 Motivation

To illustrate the rationale behind the utilization of slit sheets to create fit-for-purpose nonlinear springs, we begin by neglecting the viscoelastic component of the stiffness and the material nonlinearities. The resistive force of the kirigami spring then originates solely from geometric nonlinearities that emerge from the topological modifications introduced by the cutting patterns. The concept is best illustrated by considering a stretched membrane of length L and using a one-dimensional approximation. A kirigami spring that is stretched in its elastic region and subject to a static force F will experience a transverse displacement. The force-displacement relation can be expressed as

$$F = k\left(1 - \frac{L_o}{\sqrt{(\Delta L + L_o)^2 + x^2}}\right)x, \tag{1}$$

where k is the characteristic stiffness of the string, ΔL is the stretch in the spring due to the application of the force F, and L_0 is the unstretched length. Considering small displacements about $x = 0$, and using a Taylor's series expansion, the denominator in Eqn. (1) can be written as

$$\frac{1}{\sqrt{(\Delta L + L_o)^2 + x^2}} \approx \frac{1}{\Delta L + L_o} - \frac{x^2}{2(\Delta L + L_o)^3} + \frac{3x^4}{8(\Delta L + L_o)^3} + \mathcal{O}(x^6). \tag{2}$$

Substituting the expression in (2) into the equation in (1), the force-displacement relationship can then be approximated as

$$F \approx k\left(\left(\frac{\Delta L}{\Delta L + L_o}\right)x + \left(\frac{L_o}{2(\Delta L + L_o)^3}\right)x^3\right) + \mathcal{O}(x^5), \tag{3}$$

where $k = EA/L_{\text{eff}}$, EA is the extensional stiffness and L_{eff} is the effective length. Note that nominally $L_{\text{eff}} = \Delta L + L_o$. Examining Eqn. (3) reveals two paths to change the force-displacement relation given a fixed geometric configuration. The first is to change the stretch ΔL in the spring and the second is to modify the effective stiffness of the material (EA/L_{eff}). Assuming that EA is held constant, the concept introduced in this work is to modify k by having changes in L_{eff} through the introduction of cuts in the membrane.

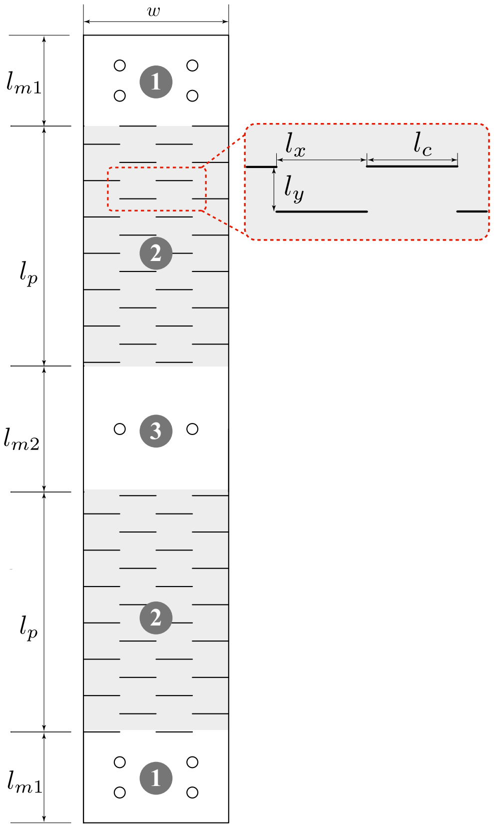

Fig. 1: An example of the proposed kirigami spring with annotated segments and dimensions. Sections in grey indicate the programmable region. Inset shows the distinctive characteristic lengths of each pattern (l_c, l_x, l_y). The specimens in this work share the following lengths l_{m1} = 30.0 mm, l_{m2} = 40.0 mm, l_p = 80.0 mm, and w = 48.0 mm.

2.1 Pattern Selection

To fully exploit the observations in the previous section, we performed a characterization of the force-displacement relationship of eight distinct kirigami patterns first introduced by Yang *et al.*[31]. Following [31], the cuts' length is designated with l_c, the horizontal spacing is l_x, while the vertical spacing is denoted as l_y (see Figure 1). It should be noted however that, due to the different loading mechanisms adopted herein, the multistable behavior of the structures observed by [31] are not retained. Nonetheless, the designation introduced in [31] provides an efficient labeling methodology to refer to the various patterns and track its influence on the force-displacement relationship.

We deliberately fixed the cut length (l_c) to 12 mm. This allowed us to reduce the number of free parameters for the design of the springs to two, i.e. the cuts' spacing l_x and l_y. Following [31], the patterns are designated by the nomenclature l_c/l_y - l_c/l_x. In this work, we considered the following patterns: 1-5, 3-2, 3-3, 3-6, 4-3, 5-1, and 5-5. We fabricated four specimens per pattern, labeled in alphabetic order from A to D. We further introduced the number of effective cuts, N_{eff}, in the tuning region (gray areas in Figure 1). This allowed us to correlate the density of the cuts with the type of constitutive equation observed. The number of effective cuts is calculated as the sum of complete and incomplete (smaller) cuts; the latter are added and rounded to a complete cut. In Figure 2 are illustrated all the patterns considered herein along with their nomenclature and the corresponding number of effective cuts.

3 Materials and methods

3.1 Fabrication

A Silhouette Cameo cutter is used to cut 260 mm long by 48 mm wide Grafix sheets (0.1778 mm nominal thickness). With reference to Fig. 1, the springs are composed of three segments: ① a mounting segment of 30 mm to ground the spring, ② an active section of 80 mm that is the *programmable (or tuning) region*, and ③ a 40 mm segment to attach the spring to a proof mass or directly apply a load. Sections 1 and 2 are mirrored about the center of the spring. Segments 1 and 3 contain mounting holes to secure the spring to ground or a mass.

3.2 Characterization of the kirigami springs stiffnesses: Quasi-Static Testing

We used a Mark-10 ESM 1500 motorized test stand to perform quasi-static, displacement-controlled tension testing. The springs were mounted on 3D-printed test stands and subjected to a 5 mm axial pre-stretch before applying the load in the transverse direction. An exemplification of the test apparatus is depicted in Figure 3a-3b. We performed five loading/unloading cycles per spring, with a displacement rate of 50 mm/min and with a maximum displacement of 30 mm. Regardless of the pattern selected, a minimal amount of hysteresis was observed between the loading and unloading curves. We, however, neglected the hysteretic behavior since the area enclosed by the hysteresis loop is considerably small.

For each spring, the constitutive relations obtained through the quasi-static test were averaged over the five loading/unloading cycles and used to calculate the stiffness coefficients. We used a curve-fitting algorithm to minimize the residual between the experimental and numerical constitutive relations (force-displacement curves). In particular, we utilized the Iteratively Reweighted Least-Squares (IRLS) method [32], which is a modified version of MATLAB *polyfit* that enables forcing a zero intercept and selectively choosing which terms of the polynomial expansions are zero (see the *polyfit* documentation for further details [1]). Motivated by the discussion that led to the equation in (3), the geometric nonlinearity is assumed elastic, and the resistive force exerted by the spring is assumed to be a cubic polynomial of the form

$$F(x) = k_1 x + k_3 x^3, \tag{4}$$

where k_1 and k_3 are respectively the linear and cubic stiffness. To derive the stiffness coefficients, we fitted the experimental data with the polynomial form of equation 4. To further verify our speculation, we performed a second fit with a complete cubic polynomial with zero intercepts and noted that the coefficient of the quadratic term was found to be considerably smaller than those of the linear and cubic terms for all patterns considered. This supports the hypothesis that the expression can be accurately represented by Equation (4). Finally, the loss mechanism is not captured in these tests and the next section presents a mechanism to quantify the structural damping.

---

[1] The "*polyfitn*" documentation is accessible through MATLAB file Exchange, full citation: John D'Errico (2024). polyfitn (`https://www.mathworks.com/matlabcentral/fileexchange/34765-polyfitn`), MATLAB Central File Exchange.

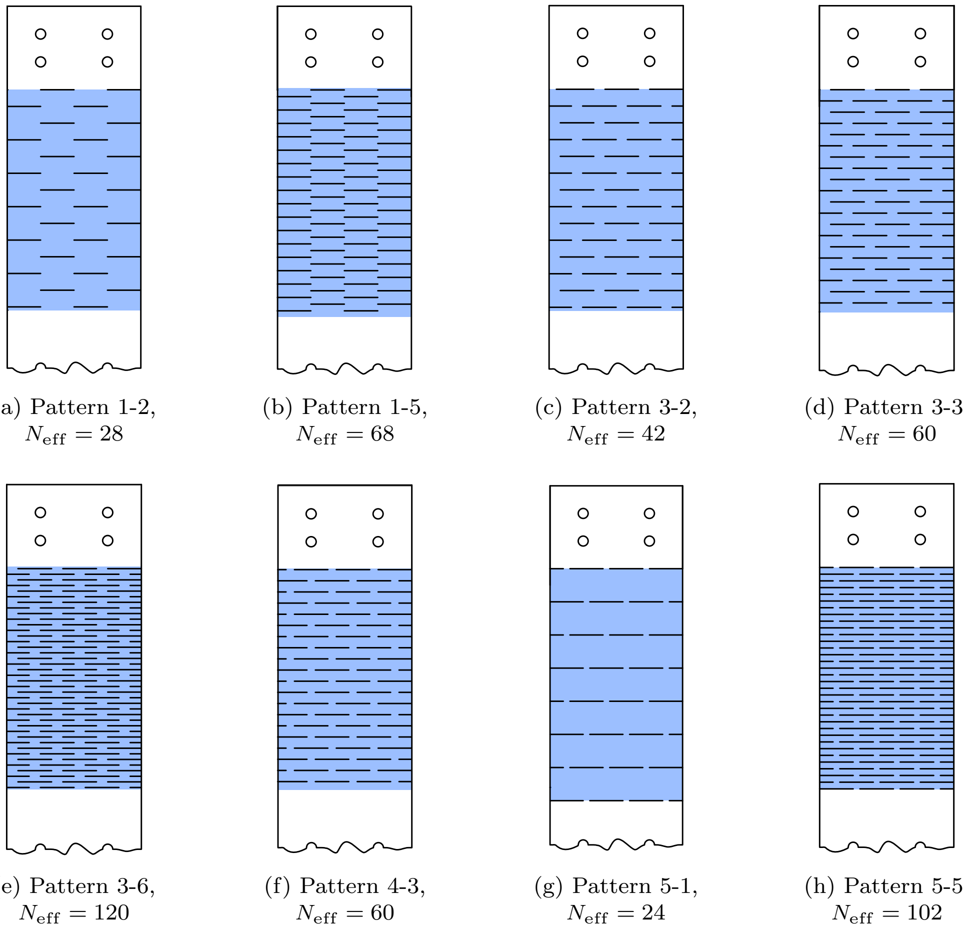

(a) Pattern 1-2, $N_{\text{eff}} = 28$
(b) Pattern 1-5, $N_{\text{eff}} = 68$
(c) Pattern 3-2, $N_{\text{eff}} = 42$
(d) Pattern 3-3, $N_{\text{eff}} = 60$
(e) Pattern 3-6, $N_{\text{eff}} = 120$
(f) Pattern 4-3, $N_{\text{eff}} = 60$
(g) Pattern 5-1, $N_{\text{eff}} = 24$
(h) Pattern 5-5, $N_{\text{eff}} = 102$

Fig. 2: Kirigami springs adopted in this work. The figure illustrates the various kirigami springs along with the pattern designation and the number of effective cuts.

3.3 Characterization of the kirigami springs stiffnesses: Transient responses

We performed modal testing to deduce the damping of the system. Differently from the quasi-static test, where each spring was tested separately, for the modal tests we arranged two springs with the same pattern in parallel and connected those to a cart that was free to oscillate on a linear air track apparatus. Equivalently to the quasi-static testing, the springs were attached to a pre-stretch mechanism (rigid bars in Figure 4) to increase the transverse stiffness of the system. A schematic representation of the test rig along with a 3D rendering of the system are depicted in Figure 4. To calculate the modal damping we speculated that the motion of the system can be described with the following nondimensional equation

$$\ddot{\chi} + \hat{c}_1\dot{\chi} + \hat{c}_2\dot{\chi}|\dot{\chi}| + \hat{c}_3\dot{\chi}^3 + \hat{k}_1\chi + \hat{k}_2\chi^2 + \hat{k}_3\chi^3 = 0, \quad (5)$$

Using the cut's length l_c as the length scale and the period of the linear system as the time scale, the nondimensional terms are defined as

$$\chi = \frac{x}{l_c}, \qquad \tau = \omega_n t, \qquad \Omega = \frac{\omega}{\omega_n}, \qquad \hat{c}_1 = \frac{c_1}{m\omega_n},$$
$$\hat{c}_2 = \frac{c_2 l_c}{m}, \quad \hat{c}_3 = \frac{c_3\omega_n l_c^2}{m}, \quad \hat{k}_2 = \frac{\bar{k}_2 l_c}{\bar{k}_1}, \quad \hat{k}_3 = \frac{\bar{k}_3 l_c^2}{\bar{k}_1}.$$

where x, $\dot{x}$, $\ddot{x}$ are respectively the displacement, velocity and acceleration of the mass, $\hat{c}_1$, $\hat{c}_2$, and $\hat{c}_3$ are the linear, quadratic and cubic damping coefficients and finally, $\hat{k}_1$, $\hat{k}_2$ and $\hat{k}_3$ are the linear, quadratic and cubic stiffness respectively. It should be noted that the coefficients $\bar{k}_i$ are the equivalent spring stiffnesses obtained as in Radomirovic *et al.* [33], calculated considering that two nonlinear springs were attached in parallel and should not be confused with the $\hat{k}_i$ which are instead the nondimensional equivalent stiffnesses. We introduced the quadratic stiffness $\bar{k}_2$ (or $\hat{k}_2$ for the nondimensional case) since the quadratic term best approximates asymmetries due to misalignment of the two

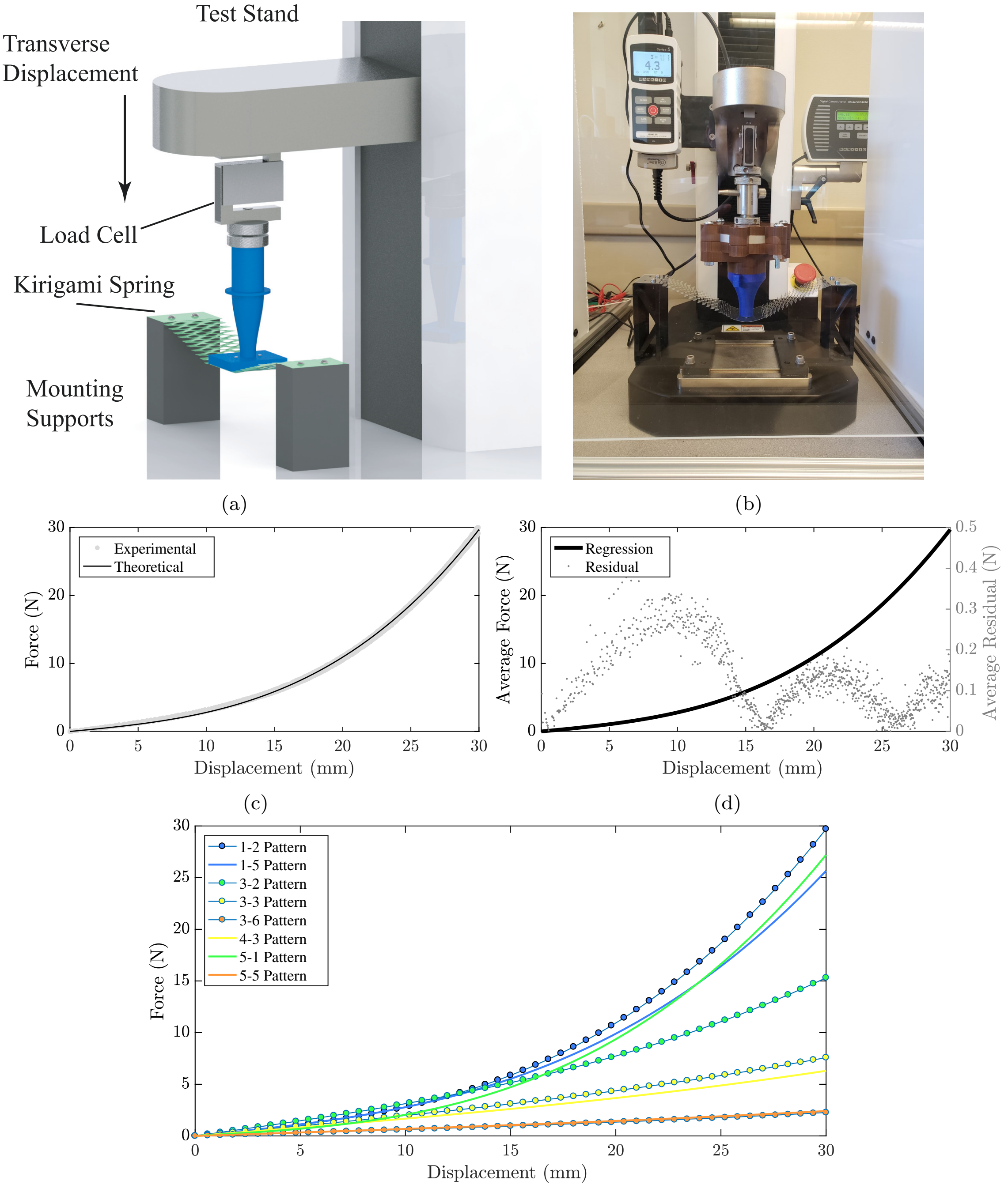

(a) (b)

(c) (d)

(e)

Fig. 3: Quasi-static characterization of kirigami springs: (a) Schematic and (b) image of force versus displacement test. (c) Theoretical and experimental force versus displacement for 1-2 pattern. (d) Theoretical fit and residual for force versus displacement for 1-2 pattern. (e) Force versus displacement relationship for all the patterns considered.

springs ([34]).

The equations of motion are in the form of a Helmholtz-Duffing oscillator with nonlinear damping [35]. While we do not anticipate that a Kirigami spring has built-in quadratic damping, we found it useful to introduce it into the equation of motion to have a meaningful physical representation of the system on the air track. Indeed, the air coming out from the air track exerts a resistive force (aerodynamic drag) onto the cart which must be considered when modeling the system.

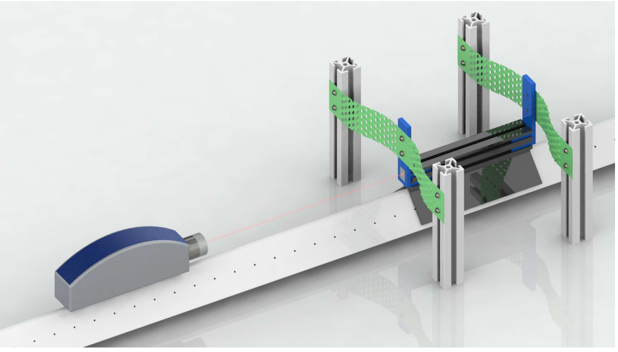

Fig. 4: Schematic of the dynamic test apparatus. The two kirigami springs (in green) are attached to the sliding mass through the 3D printed support (blue) and to the pre-stretch system (vertical bar). The velocity of the system was measured with the Polytec OFV-534 Laser vibrometer; the Data Physics Abacus DP 901-6C DSP acquisition system, not depicted in the figure, completed the experimental set-up.

A cursory inspection of the equation (5) unveils the presence of four unknowns that must be determined to fully characterize the system. To calculate the unknown coefficients $C_i = \{\hat{k}_2,\ \hat{c}_1,\ \hat{c}_2,\ \hat{c}_3\}$, we cast the system identification problem into a minimization problem, stated as follows:

$$\min_{C^i} \sum_{t\in[0,10]} \Big(\dot{\chi}(t) - \dot{x}(t)\Big)^2 \max\Big(|\dot{\chi}(t) - \dot{x}(t)|\Big),$$

$$\textbf{subject to:} \qquad (6)$$

$$\hat{k}_3 \leq \hat{k}_2 \leq \hat{k}_1, \qquad 0 \leq \hat{c}_1 \leq \eta\ \hat{c}_{cr},$$
$$0 \leq \hat{c}_2 \leq \eta\ \hat{c}_{cr}, \qquad 0 \leq \hat{c}_3 \leq \eta\ \hat{c}_{cr}.$$

where $\dot{x}(t)$ is the experimental time history while $\dot{\chi}(t)$ is the numerical time history, $\hat{k}_2$ is the quadratic stiffness coefficient, $\hat{c}_1,\ \hat{c}_2,\ \hat{c}_3$ are the damping coefficients and $\eta \ll 1$ is a small parameter that ensures that the damping coefficients are smaller than the critical value. Due to non-dimensionalization, $\hat{k}_1 = 1$ for all the springs. While the first term of the functional to be minimized is to ensure that the experimental and numerical response have the same waveform, the second term simply forces the peaks of the numerical response to be in-phase with that of the experimental response. For the optimization, we used only the first 10 seconds of the experimental time-history. We solved the nonlinear constrained optimization problem using the MATLAB built-in function *fmincon*, notably by adopting the interior-point algorithm. The results of the optimization are detailed in Section 5. We further compared the amplitude of vibrations obtained experimentally and numerically with those calculated with the Method of Multiple Time Scales. The details of the derivation are reported in Appendix C. The comparison extends to a time history of 25 seconds; this is to demonstrate that the parameters identified characterize the systems beyond the 10 seconds used for the optimization.

4 Forced vibrations

In this section, we calculate uniformly valid solutions for the equation in (7) using the Method of Multiple Time Scales. We begin by reorganizing the equation of motion by introducing a bookkeeping parameter ε and collecting terms of the same order. The equation of motion can be written as follows

$$\ddot{\chi} + \chi + \varepsilon\hat{k}_2\chi^2 + \varepsilon^2\left(\hat{k}_3\chi^3 + \hat{c}_1\dot{\chi} + \hat{c}_2\dot{\chi}|\dot{\chi}| + \hat{c}_3\dot{\chi}^3\right) = \varepsilon^2 a_b\cos(\Omega t). \qquad (7)$$

Note that the damping coefficients and the cubic stiffness are scaled at order ϵ^2 and the quadratic stiffness term is scaled on the order of ϵ. This implies that the following inequality must hold $\hat{k}_3 < \hat{k}_2 < \hat{k}_1$ for the asymptotic solution presented below to be valid.
The time dependence is expanded into multiple scales $T_n = \epsilon^n\tau$, and the time derivatives can be written as

$$\frac{\partial}{\partial t} = D_0 + \varepsilon D_1 + \varepsilon^2 D_2 + \mathcal{O}(\varepsilon^3), \qquad (8a)$$
$$\frac{\partial^2}{\partial t^2} = D_0^2 + 2\varepsilon D_0 D_1 + \varepsilon^2\left(D_1^2 + 2D_0D_2\right) + \mathcal{O}(\varepsilon^3), \qquad (8b)$$

where $D_n = \partial/\partial T_n$. Furthermore, the time-dependent non-dimensional displacement χ can be expressed as

$$\chi(t;\varepsilon) = \sum_{i=0}^{2}\varepsilon^i\chi_i(T_0, T_1, T_2) + \mathcal{O}(\varepsilon^3). \qquad (9)$$

Substituting Eqns.(8) and (9) in the Eqn.(7) and gathering terms with the same power of ε yields

$$\mathcal{O}(\varepsilon^0) : D_0^2\chi_0 + \chi_0 = 0, \qquad (10a)$$
$$\mathcal{O}(\varepsilon^1) :\ D_0^2\chi_1 + \chi_1 = -2D_0D_1\chi_0 - \hat{k}_2\chi_0^2, \qquad (10b)$$
$$\mathcal{O}(\varepsilon^2) :\ D_0^2\chi_2 + \chi_2 = -2D_0D_1\chi_1 - D_1^2\chi_0 \qquad (10c)$$
$$- 2D_0D_2\chi_0$$
$$- 2\hat{k}_2\chi_0\chi_1 - \hat{k}_3\chi_0^3 - \hat{c}_1D_0\chi_0 - \hat{c}_3(D_0\chi_0)^3$$
$$- \hat{c}_2\left(g_1\exp(iT_0)\ \mathrm{d}T_0 + \sum_{\substack{-\infty\\ n\neq 1}}^{\infty} g_n\exp(inT_0)\right)$$
$$+ a_B\cos(\omega_0T_0 + \sigma T_2).$$

We let the excitation interact at the same order of the nonlinear damping and the cubic stiffness and, for consistency, assumed

$$\omega_0 = \omega_n + \varepsilon^2\sigma \qquad (11)$$

where σ is the detuning parameter. Solutions to the $\mathcal{O}(\varepsilon^0)$ expansion in Eqn. (10a) can be written as

$$\chi_0 = A(T_1, T_2)\exp\left(iT_0\right) + \bar{A}(T_1, T_2)\exp\left(-iT_0\right), \quad (12)$$

where $\bar{A}$ is the complex conjugate of A. Substituting into Eqn. (10b) yields

$$\begin{aligned} D_0^2\chi_1 + \chi_1 = &- 2iD_1A\exp(iT_0) - \hat{k}_2A^2\exp(2iT_0) \\ &- \hat{k}_2A\bar{A} + cc, \end{aligned} \quad (13)$$

where cc denotes complex conjugate. To derive a uniformly valid expansion, we must eliminate secular terms from Eqn. (13) hence, $D_1A = 0$; therefore, $A = A(T_2)$. The solution to Eqn. (13) can be written as

$$\chi_1 = \hat{k}_2\left(\frac{A^2}{3}\exp(2iT_0) - A\bar{A}\right) + cc. \quad (14)$$

Substituting the latter in the equation in (10c), one has

$$\begin{aligned} &D_0^2\chi_2 + \chi_2 = \\ &\Bigg(2iD_2A + i\hat{c}_1A + \frac{i\hat{c}_2A^2}{2\pi}\int_0^{2\pi}\sin^2(\phi)\big|\sin(\phi)\big|\mathrm{d}\phi \\ &+ 3i\hat{c}_3A^2\bar{A} + 3k_3A^2\bar{A} + \tfrac{10}{3}\hat{k}_2^2A^2\bar{A} + \\ &\tfrac{a_B}{2}\exp(\sigma T_2)\Bigg)\exp(iT_0) \\ &- \Bigg(2\hat{k}_2^2A^2\left(\tfrac{A}{3} + 2\bar{A}\right) - \hat{k}_3A^3 - i\hat{c}_1A^3 \\ &- i\hat{c}_3A^3\Bigg)\exp(3iT_0) - \hat{c}_2\sum_{\substack{-\infty \\ n\neq 1}}^{\infty} g_n\exp(inT_0). \end{aligned} \quad (15)$$

Secular terms can be eliminated if

$$\begin{aligned} &\Bigg(2iD_2A + i\hat{c}_1A + \frac{i\hat{c}_2A^2}{2\pi}\int_0^{2\pi}\sin^2(\phi)\big|\sin(\phi)\big|\mathrm{d}\phi \\ &\quad + 3i\hat{c}_3A^2\bar{A} + 3k_3A^2\bar{A} + \tfrac{10}{3}\hat{k}_2^2A^2\bar{A} + \tfrac{a_B}{2}\exp(\sigma T_2)\Bigg). \end{aligned} \quad (16)$$

Letting $A = a\exp(i\beta)$ and separating real and imaginary parts yields

$$\dot{a} = -\frac{\hat{c}_1}{2}a - \frac{4\hat{c}_2}{3\pi}a^2 - \frac{3\hat{c}_3}{8}a^3 + \frac{a_B}{2}\sin\big(\sigma T_2 - \beta\big), \quad (17a)$$

$$a\dot{\beta} = \frac{10k_2^2 - 9k_3}{24}a^3 - \frac{a_B}{2}\cos\big(\sigma T_2 - \beta\big). \quad (17b)$$

Defining $\gamma = \sigma T_2 - \beta$, differentiating with respect to T_2 and substituting into the modulation equations 17b one has

$$\dot{a} = -\frac{\hat{c}_1}{2}a - \frac{4\hat{c}_2}{3\pi}a^2 - \frac{3\hat{c}_3}{8}a^3 + \frac{a_B}{2}\sin\big(\gamma\big), \quad (18a)$$

$$a\dot{\gamma} = a\sigma - \frac{10k_2^2 - 9k_3}{24}a^3 + \frac{a_B}{2}\cos\big(\gamma\big). \quad (18b)$$

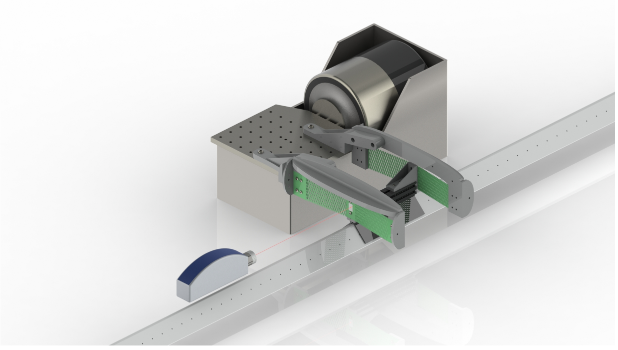

Fig. 5: Schematic of the dynamic test apparatus utilized for the forced responses. The two kirigami springs (in green) are attached to the sliding mass through the 3D printed supports which include also the prestretch mechanism for the springs. The base accelerations were provided by the Labworks Inc. DB 139 - DuoBase shaker table, and were measured utilizing a PCB accelerometer. The velocity of the system was measured using the Polytec OFV-534 Laser vibrometer.

Steady-state motion occurs when $\dot{\alpha}, \dot{\gamma} = 0$. We found it convenient to define the following term

$$\mu_{NL} = -\frac{\hat{c}_1}{2}a - \frac{4\hat{c}_2}{3\pi}a^2 - \frac{3\hat{c}_3}{8}a^3. \quad (19)$$

Next, squaring and adding the two equations in (18) one has

$$\sigma = \frac{10k_2^2 - 9k_3}{24}a^2 \pm \sqrt{\frac{a_B}{4a^2} - \mu_{NL}^2}. \quad (20)$$

The test apparatus used to test the kirigami springs subjected to harmonic excitation is illustrated in Figure 5.

5 Results and Discussion

We begin by reporting the results concerning the quasi-static characterization of the spring, i.e. the 3-point bending tests performed to deduce k_1 and k_3 (see Figure 3). In the interest of brevity, in this section, we report only the results pertaining the average and standard deviation for the various patterns considered. The results per specimens are detailed in the Appendix B (see Table B.1). The values of the quadratic coefficients when the experimental data are fitted with a polynomial of the type: $F = k_1x + k_2x^2 + k_3x^3$, are reported in the Appendix B. Here quadratic nonlinearities are imputable to asymmetries due to imprecise manufacturing of the slits; however, a cursory inspection of the

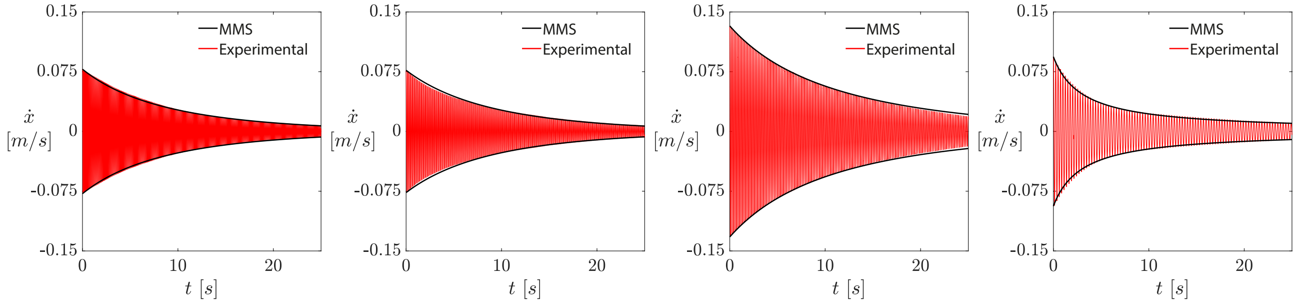

(a) Pattern 1-2 (b) Pattern 3-2 (c) Pattern 3-3 (d) Pattern 3-6

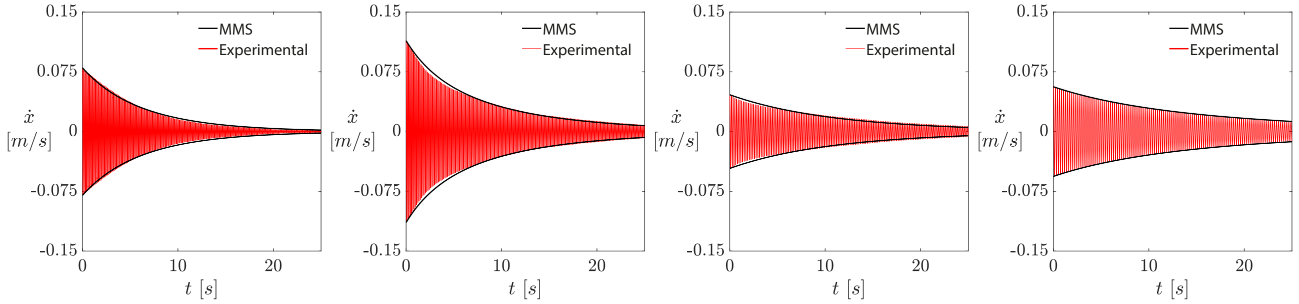

(e) Pattern 1-5 (f) Pattern 5-1 (g) Pattern 4-3 (h) Pattern 5-5

Fig. 6: Comparison of the experimental time responses against the amplitude of vibrations as predicted using the Method of Multiple Time Scales for all the springs of the BC series. The experimental time responses are in red, amplitudes of vibrations obtained by the method of multiple time scales are in black (see Appendix C for a more detailed explanation).

Table reveals that the quadratic terms are negligible compared to the linear and cubic stiffness coefficients. This verifies our hypothesis that a cubic polynomial with odd powers and zero intercept best represents the physics of the deformation for the quasi-static test.
Table 1 reports the averaged linear and cubic stiffness and the corresponding standard deviation in their values obtained from the quasi-static tests. The results in Table 1 are the averaged stiffness per cycle and specimen. It is worth noting that, the standard deviation for each of the specimens tested is two orders of magnitude lower than the average value, implying that the springs' responses are consistent among the various specimens. Hence, it could be concluded that there is a good correlation between the slit pattern selected and the constitutive equation determined. In general, patterns with larger cut densities, for instance, 5-5 and 3-6, are more compliant than other patterns. One could compare the stiffnesses obtained for the spring 5-5 and 3-2 and notice that both the linear and the cubic stiffnesses differ of an order of magnitude. This is due to the higher cut density of the spring 5-5 compared to the spring 3-2.

Table 1: Mean and standard deviation of the experimental linear and cubic stiffness for each spring pattern. The results are averaged per loading cycle and per specimen.

Pattern	**k_1 (N/mm)**		**k_3 (N/mm^3)**	
	Average	Standard Deviation	Average	Standard Deviation
1-2	0.1912	7.978E-3	8.878E-4	1.371E-5
1-5	0.2061	9.597E-3	7.213E-4	1.463E-5
3-2	0.2877	8.847E-3	2.472E-4	3.537E-5
3-3	0.1913	4.917E-3	6.818E-5	6.887E-6
3-6	0.0597	4.949E-3	1.750E-5	7.666E-7
4-3	0.1620	1.047E-2	5.353E-5	4.902E-6
5-1	0.1172	4.096E-3	8.770E-4	1.120E-5
5-5	0.0663	2.295E-3	1.559E-5	1.444E-6

In Table 1, we only reported the values for the linear and cubic springs. To fully characterize the system and, in particular, its transient behavior, we cast a system identification problem into a constrained optimization problem, as detailed in section 3.3. For all the systems analyzed, the optimum values for the quadratic spring term and the damping coefficients resulting from the nonlinear constrained minimization problem are reported in Table 2. The reason for re-introducing the quadratic stiffness in the dynamical model was already discussed in Section 3.3. While for the quasi-static testing the quadratic term was only imputable to asymmetries in the single spring, here the significance of k_2 is to model the misalignments when the two springs are mounted in parallel. Since there is not a closed form expression that can capture the springs' misalignment, k_2 is adjoined to the set of optimization parameters. For completeness, we report in Table 2 also the non-dimensional cubic stiffness; note that, the non-dimensional linear stiffnesses $\hat{k}_1 = 1$ for all the systems considered and thus are not included in Table 2. A cursory inspection of the quadratic stiffness terms for the various systems unveils that they are inversely proportional to k_3. The random nature of the quadratic stiffness terms and their limited variability compared to $\hat{k}_1$ and $\hat{k}_3$ allow us to conclude that the quadratic term is unrelated to the kirigami pattern and is mainly due to misalignment of the two springs, as speculated above.

Table 2: Non-dimensional parameters for the various systems considered in the present study. The results pertain to the BC series. The non-dimensional linear spring stiffness is $\hat{k}_1 = 1$ for all the systems considered.

Pattern	$\hat{k}_2$	$\hat{k}_3$	$\hat{c}_1$	$\hat{c}_2$	$\hat{c}_3$
1-2	3.4609E-1	3.8998E-2	2.7999E-3	3.5159E-3	6.1803E-4
1-5	3.8948E-2	4.2529E-2	5.6999E-3	1.5304E-3	1.1713E-3
3-2	4.3608E-2	1.4387E-2	3.5599E-3	2.8928E-3	3.3471E-4
3-3	2.2639E-1	7.1657E-3	2.5999E-3	2.4246E-3	2.3515E-4
3-6	3.3564E-1	3.8560E-3	1.9993E-4	2.3226E-2	1.7980E-3
4-3	2.0242E-1	6.7939E-3	4.8043E-3	1.2186E-3	7.2505E-5
5-1	4.1282E-2	5.4289E-2	3.3999E-3	5.0544E-3	7.5140E-5
5-5	1.8475E-1	2.7833E-3	3.2011E-3	2.9852E-3	2.3884E-4

Next, we compare the amplitude of vibrations calculated with the method of multiple scales (as detailed in the appendix C) against the experimental results. Although we used only the first order approximation, i.e χ_0, and regardless of the pattern considered, we found that the predicted and measured amplitude are in good agreement (see Figure 6). The various shapes of the amplitude-time response highlight how the various patterns offer remarkably different dynamical responses, therefore emphasizing the degree of programmability achievable through kirigami slits.

The experimental results concerning the forced vibrations for the springs 3-6 and 4-3 are reported in Figure 7. Without loss in generality, we tested the pair BC. The experimental responses were obtained using the setup depicted in Figure 5. We performed a frequency sweep (0.002 Hz/sec) in the neighborhood of the primary resonance and excited the system with harmonic motion of the base with acceleration a_b= 0.05 g, 0.1 g, and 0.2 g respectively. We believe that the discrepancy between the amplitude predicted by the Method of Multiple Time Scales and the experimental results can be attributed to nonlinear damping, specifically quadratic damping due to aerodynamic drag. This quadratic damping is likely influenced by two primary factors: asymmetries in the system and the velocity at which the system vibrates. The velocity dependence is analogous to what is observed in airfoils, where the drag coefficient varies with the Reynolds number. In contrast, the impact of asymmetries is expected to be only weakly dependent on velocity. Given that the system's velocity during the transient response is much lower than during forced vibrations, we contend that the quadratic damping measured in the transient response provides a more accurate estimate of the system's intrinsic damping. Therefore, fitting the damping again to match the experimental response under forced vibrations falls beyond the scope of this study. Nonetheless, our approach successfully captures the shape of the backbone curve, the frequency at which the jump occurs, and, within an acceptable margin, the amplitude of the system's vibrations.

The current analysis reveals that the density of the cuts is the leading parameter that influences the response of the springs. Notably, the cuts density influences the rigidity of the kirigami springs, the higher the density, the more compliant the spring. Moreover, springs with higher cuts density exhibit a quasi-linear behavior in the static test. This can be seen from Figure 3e, particularly for the patterns 5-5, 3-6, and 4-3. As the density decreases the nonlinear behavior is more pronounced; this is likely due to post-buckling experienced by the single slit. Interestingly, the transient responses of the springs with patterns 3-6, 4-3, and 5-5 exhibit significant deviations from the standard exponential decay. Specifically, these springs demonstrate a more complex decay behavior characterized by non-exponential damping effects. The observed responses suggest the presence of higher-order damping terms that dominate the transient decay behavior, leading to a more gradual attenuation of oscillations over time for patterns 4-3 and 5-5, or a more pronounced attenuation for pattern 3-6. These observations are corroborated by the current model.

The possibility of controlling the constitutive response and designing system whose stiffness and damping properties can be tuned, may find application in the design of wearable electronics, adaptive aerospace structures, soft-robotics, vibration-isolation for precision devices, to name but a few. Moreover, the relatively inexpensive set up, and its simplicity renders the system ideal for educational purposes.

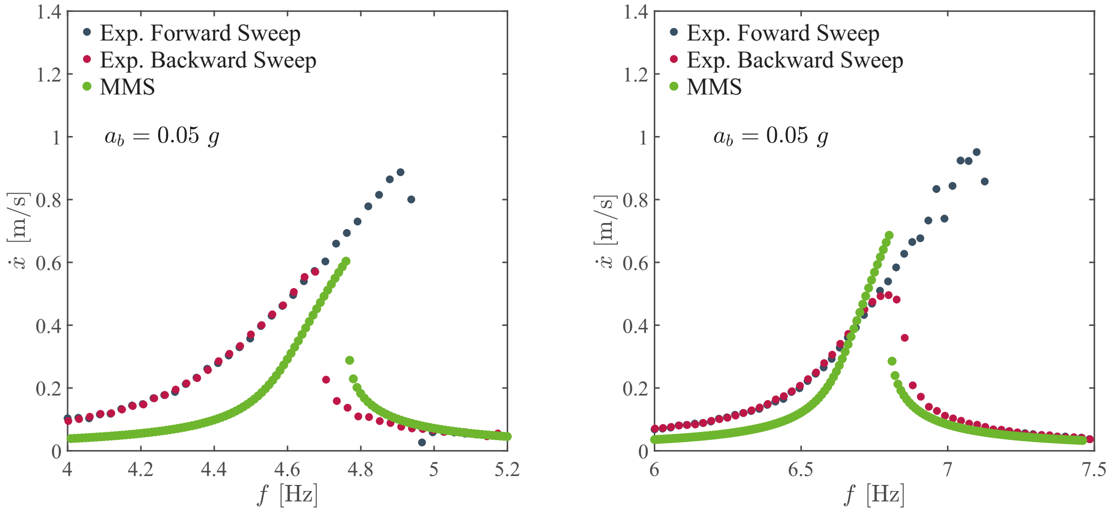

(a) Pattern 3-6 $a_b = 0.05g$ (b) Pattern 4-3 $a_b = 0.05g$

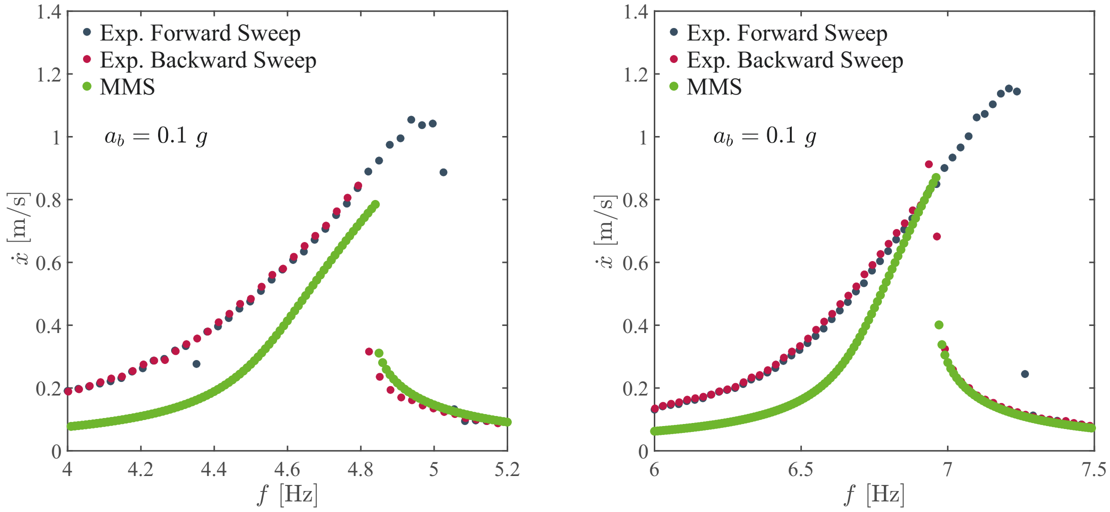

(c) Pattern 3-6 $a_b = 0.1g$ (d) Pattern 4-3 $a_b = 0.1g$

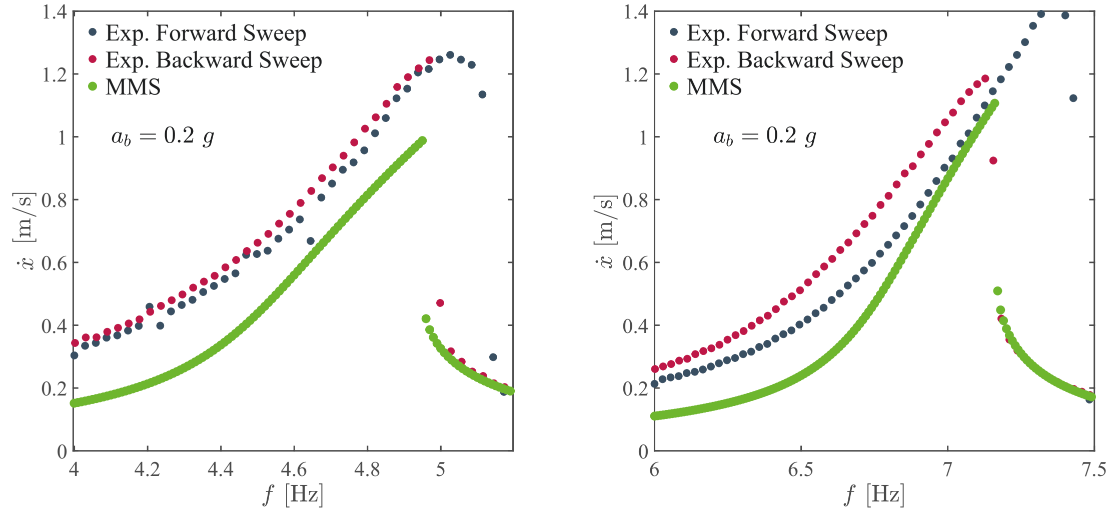

(e) Pattern 3-6 $a_b = 0.2g$ (f) Pattern 4-3 $a_b = 0.2g$

Fig. 7: Comparison of the experimental time responses against the amplitude of vibrations as predicted using the Method of Multiple Time Scales for the spring pattern 3-6 and 4-3 respectively. Unstable solutions not shown in the figure. Figure (a), (c) and (e) are the response for the 3-6 pattern with excitation level of respectively 0.05 g, 0.1 g, and 0.2 g. Likewise, figure (b), (d) and (f) are for the 4-3 pattern with excitation level of respectively 0.05 g, 0.1 g, and 0.2 g.

5.1 Limitations and concluding remarks

The following limitations are noteworthy

- In the model, the viscoelastic behavior of the constitutive material and the effect of fatigue in the plastic hinges were neglected.
- The approximation for the constitutive relationship was truncated to the third order. This decision is motivated by the excellent agreement between the experimental data and the curve fitting achieved by retaining only the linear and cubic terms. Springs more compliant than those considered here may require a different polynomial form.
- The effect of quadratic nonlinearities was included to account for the misalignment of the two springs when assembled to form the single-degree-of-freedom system. Quadratic nonlinearities may also emerge in the presence of manufacturing imperfections. To address this, experimental data would need to be fitted with a complete third-order polynomial instead of a polynomial with only odd powers. Our approach implicitly assumes that the springs are manufactured without imperfections or asymmetries, and that misalignment of the spring pairs is the sole source of imperfection. This explains why, in this case, quadratic terms appear only when the system is assembled to form the single DOF oscillator.
- It is hypothesized that the kirigami springs exhibit nonlinear damping that can be represented in polynomial form. This choice is deliberate, based on the assumption that the damping behavior mirrors that of stiffness.
- The quadratic damping is considered to arise solely from the resistive aerodynamic force exerted on the oscillator by the airflow from the air truck. Errors may arise from the almost inevitable torques exerted on the oscillator cart due to any misalignment among the parallel kirigami springs and the air track, especially under large-amplitude vibrations. The torques may lead to pitch or yaw of the cart body, both of which can potentially reshape or even close the air channels to complicate the damping mechanism.

Acknowledgements The authors would like to acknowledge the financial support provided by NSF CAREER Award: CMMI 2145803 and the Purdue Research Foundation (PRF).

Conflict of interest

The authors declare that they have no conflict of interest.

References

Bruton, J. T., T. G. Nelson, T. K. Zimmerman, J. D. Fernelius, S. P. Magleby, and L. L. Howell (2016). “Packing and deploying Soft Origami to and from cylindrical volumes with application to automotive airbags”. In: *Royal Society open science* 3.9, p. 160429.

Sargent, B., J. Butler, K. Seymour, D. Bailey, B. Jensen, S. Magleby, and L. Howell (2020). “An origami-based medical support system to mitigate flexible shaft buckling”. In: *Journal of Mechanisms and Robotics* 12.4.

Faber, J. A., A. F. Arrieta, and A. R. Studart (2018). “Bioinspired spring origami”. In: *Science* 359.6382, pp. 1386–1391.

Yang, Y., K. Vella, and D. P. Holmes (2021). “Grasping with kirigami shells”. In: *Science Robotics* 6.54, eabd6426.

Ai, C., Y. Chen, L. Xu, H. Li, C. Liu, F. Shang, Q. Xia, and S. Zhang (2021). “Current Development on Origami/Kirigami-Inspired Structure of Creased Patterns toward Robotics”. In: *Advanced Engineering Materials* 23.10, p. 2100473. DOI: `https://doi.org/10.1002/adem.202100473`.

Jin, L., A. E. Forte, B. Deng, A. Rafsanjani, and K. Bertoldi (2020). “Kirigami-inspired inflatables with programmable shapes”. In: *Advanced Materials* 32.33, p. 2001863.

Callens, S. J. and A. A. Zadpoor (2018). “From flat sheets to curved geometries: Origami and kirigami approaches”. In: *Materials Today* 21.3, pp. 241–264. ISSN: 1369-7021. DOI: `https://doi.org/10.1016/j.mattod.2017.10.004`.

Castle, T., Y. Cho, X. Gong, E. Jung, D. M. Sussman, S. Yang, and R. D. Kamien (2014). “Making the Cut: Lattice Kirigami Rules”. In: *Phys. Rev. Lett.* 113 (24), p. 245502. DOI: `10.1103/PhysRevLett.113.245502`.

Rafsanjani, A., Y. Zhang, B. Liu, S. M. Rubinstein, and K. Bertoldi (2018). “Kirigami skins make a simple soft actuator crawl”. In: *Science Robotics* 3.15, eaar7555.

Rafsanjani, A., L. Jin, B. Deng, and K. Bertoldi (2019). “Propagation of pop ups in kirigami shells”. In: *Proceedings of the National Academy of Sciences* 116.17, pp. 8200–8205.

Saito, K., F. Agnese, and F. Scarpa (2011). “A Cellular Kirigami Morphing Wingbox Concept”. In: *Journal of Intelligent Material Systems and Structures* 22.9, pp. 935–944. DOI: `10.1177/1045389X11416030`.

Lamoureux, A., K. Lee, M. Shlian, S. R. Forrest, and M. Shtein (2015). “Dynamic kirigami structures for integrated solar tracking”. In: *Nature Communica-*

tions 6.1, p. 8092. ISSN: 2041-1723. DOI: `10.1038/ncomms9092`.

Dias, M. A., M. P. McCarron, D. Rayneau-Kirkhope, P. Z. Hanakata, D. K. Campbell, H. S. Park, and D. P. Holmes (2017). “Kirigami actuators”. In: *Soft Matter* 13 (48), pp. 9087–9092. DOI: `10.1039/C7SM01693J`.

Zheng, C., H. Oh, L. Devendorf, and E. Y.-L. Do (2019). “Sensing Kirigami”. In: *Proceedings of the 2019 on Designing Interactive Systems Conference*. DIS ’19. San Diego, CA, USA: Association for Computing Machinery, 921–934. ISBN: 9781450358507. DOI: `10.1145/3322276.3323689`.

Zhai, Z., L. Wu, and H. Jiang (Nov. 2021). “Mechanical metamaterials based on origami and kirigami”. In: *Applied Physics Reviews* 8.4, p. 041319. ISSN: 1931-9401. DOI: `10.1063/5.0051088`.

Tang, Y., G. Lin, S. Yang, Y. K. Yi, R. D. Kamien, and J. Yin (2017). “Programmable kiri-kirigami metamaterials”. In: *Advanced Materials* 29.10, p. 1604262.

Sussman, D. M., Y. Cho, T. Castle, X. Gong, E. Jung, S. Yang, and R. D. Kamien (2015). “Algorithmic lattice kirigami: A route to pluripotent materials”. In: *Proceedings of the National Academy of Sciences* 112.24, pp. 7449–7453. DOI: `10.1073/pnas.1506048112`.

Sun, Y., W. Ye, Y. Chen, W. Fan, J. Feng, and P. Sareh (2021). “Geometric design classification of kirigami-inspired metastructures and metamaterials”. In: *Structures* 33, pp. 3633–3643. ISSN: 2352-0124. DOI: `https://doi.org/10.1016/j.istruc.2021.06.072`.

Tang, Y. and J. Yin (2017). “Design of cut unit geometry in hierarchical kirigami-based auxetic metamaterials for high stretchability and compressibility”. In: *Extreme Mechanics Letters* 12. Frontiers in Mechanical Metamaterials, pp. 77–85. ISSN: 2352-4316. DOI: `https://doi.org/10.1016/j.eml.2016.07.005`.

de Magalhães Santos, G. B., L. F. Soares, A. J. B. Campuzano, R. J. da Silva, C. T. Garcia, T. H. Panzera, and F. Scarpa (2024). “Double-arrowhead castor-oil biobased polyurethane foam metamaterials”. In: *Industrial Crops and Products* 218, p. 118828. ISSN: 0926-6690. DOI: `https://doi.org/10.1016/j.indcrop.2024.118828`.

Soleimani, H., T. Goudarzi, and M. Aghdam (2021). “Advanced structural modeling of a fold in Origami/Kirigami inspired structures”. In: *Thin-Walled Structures* 161, p. 107406. ISSN: 0263-8231.

Danzi, F., J. Jenkins, H. Tao, and J. M. Gibert (Aug. 2022). “Characterization of Nonlinear Kirigami Springs Through Transient Response”. In: vol. Volume 9: 18th International Conference on Multibody Systems, Nonlinear Dynamics, and Control (MSNDC). International Design Engineering Technical Conferences and Computers and Information in Engineering Conference, V009T09A009. DOI: `10.1115/DETC2022-93913`.

Zhu, R, H Yasuda, G. Huang, and J. Yang (2018). “Kirigami-based elastic metamaterials with anisotropic mass density for subwavelength flexural wave control”. In: *Scientific reports* 8.1, pp. 1–11.

Gandla, S., J. Song, J. Shin, S. Baek, M. Lee, D. Khan, K.-Y. Lee, J. H. Kim, and S. Kim (2021). “Mechanically Stable Kirigami Deformable Resonant Circuits for Wireless Vibration and Pressure Sensor Applications”. In: *ACS Applied Materials & Interfaces* 13.45, pp. 54162–54169.

Chen, B. G.-g., B. Liu, A. A. Evans, J. Paulose, I. Cohen, V. Vitelli, and C. D. Santangelo (2016). “Topological Mechanics of Origami and Kirigami”. In: *Phys. Rev. Lett.* 116 (13), p. 135501. DOI: `10.1103/PhysRevLett.116.135501`.

Tao, J., H. Khosravi, V. Deshpande, and S. Li (2023). “Engineering by Cuts: How Kirigami Principle Enables Unique Mechanical Properties and Functionalities”. In: *Advanced Science* 10.1, p. 2204733. DOI: `https://doi.org/10.1002/advs.202204733`.

Moshe, M., E. Esposito, S. Shankar, B. Bircan, I. Cohen, D. R. Nelson, and M. J. Bowick (2019). “Kirigami Mechanics as Stress Relief by Elastic Charges”. In: *Phys. Rev. Lett.* 122 (4), p. 048001. DOI: `10.1103/PhysRevLett.122.048001`.

Hong, Y., Y. Chi, S. Wu, Y. Li, Y. Zhu, and J. Yin (2022). “Boundary curvature guided programmable shape-morphing kirigami sheets”. In: *Nature Communications* 13.1, p. 530. DOI: `10.1038/s41467-022-28187-x`.

Wang, C., J. Li, and D. Zhang (2023). “Motion singularity analysis of the thick-panel kirigami”. In: *Mechanism and Machine Theory* 180, p. 105162. ISSN: 0094-114X. DOI: `https://doi.org/10.1016/j.mechmachtheory.2022.105162`.

McMahan, C., A. Akerson, P. Celli, B. Audoly, and C. Daraio (2022). “Effective continuum models for the buckling of non-periodic architected sheets that display quasi-mechanism behaviors”. In: *Journal of the Mechanics and Physics of Solids* 166, p. 104934. ISSN: 0022-5096. DOI: `https://doi.org/10.1016/j.jmps.2022.104934`. URL: `https://www.sciencedirect.com/science/article/pii/S0022509622001314`.

Yang, Y., M. A. Dias, and D. P. Holmes (2018). “Multistable kirigami for tunable architected materials”. In: *Physical Review Materials* 2.11, p. 110601.

Holland, P. W. and R. E. Welsch (1977). “Robust regression using iteratively reweighted least-squares”. In: *Communications in Statistics - Theory and Methods* 6.9, pp. 813–827.

Radomirovic, D. and I. Kovacic (2015). “An equivalent spring for nonlinear springs in series”. In: *European Journal of Physics* 36.5, p. 055004.

Lacarbonara, W. (2013). *Nonlinear Structural Mechanics: Theory, Dynamical Phenomena and Modeling.* Springer Publishing Company, Incorporated. ISBN: 1441912754.

Kovacic, I. and G. Gatti (2018). “Helmholtz, duffing and helmholtz-duffing oscillators: exact steady-state solutions”. In: *IUTAM Symposium on Exploiting Nonlinear Dynamics for Engineering Systems.* Springer, pp. 167–177.

Appendix A List of Symbols

Symbol	Definition
F	Force applied to the kirigami spring.
k	Characteristic stiffness of the spring.
L_0	Unstretched length of the spring.
ΔL	Stretch in the spring due to the applied force.
x	Transverse displacement of the spring.
E	Extensional stiffness of the material.
A	Cross-sectional area of the spring.
L_{eff}	Effective length of the spring.
N_{eff}	Number of effective cuts in the kirigami spring.
c_1	Linear damping coefficient.
c_2	Quadratic damping coefficient.
c_3	Cubic damping coefficient.
k_1	Linear stiffness coefficient.
k_2	Quadratic stiffness coefficient.
k_3	Cubic stiffness coefficient.
χ	Nondimensional displacement.
τ	Nondimensional time.
ω_n	Natural frequency of the linear system.
Ω	Nondimensional frequency.
σ	Detuning parameter.
ϵ	Bookkeeping parameter used in the perturbation analysis.
T_n	Multiple time scales for perturbation analysis.
γ	Phase difference in the modulation equations.
a	Amplitude of oscillation.
a_{B}	Base acceleration.
β	Phase of oscillation.
μ_{NL}	Nonlinear damping term.
$\hat{k}_1, \hat{k}_2, \hat{k}_3$	Nondimensional stiffness coefficients for linear, quadratic, and cubic stiffness respectively.
$\hat{c}_1, \hat{c}_2, \hat{c}_3$	Nondimensional damping coefficients for linear, quadratic, and cubic damping respectively.
g_n	Fourier coefficients used in approximating the function $\dot{x}\lvert\dot{x}\rvert$.

Appendix B Quasi-static characterization

Here we report the results of the curve-fitting method utilized to calculate the linear k_1, and cubic k_3 stiffnesses. The results are detailed for any of the four specimens manufactured per pattern. For each specimen, the values reported in the third and fourth columns are averaged among the five loading cycles. The values reported in the column from fifth to eighth are averaged for all the specimens.

Table B.1: Experimental results of the quasi-static characterization.

Pattern	**Specimen**	k_1 N/mm	k_3 N/mm	**Average** k_1 N/mm	**St. dev.** k_1 N/mm	**Average** k_3 N/mm	**St. dev.** K_3 N/mm
1,2	a	-	-	0.1912	7.978E-3	8.8781E-04	1.3710E-05
	b	0.1844	8.7460E-04				
	c	0.2000	8.8685E-04				
	d	0.1893	9.0197E-04				
1,5	a	0.2079	7.2962E-04	0.2061	9.597E-3	7.2126E-04	1.4629E-05
	b	0.2114	7.3012E-04				
	c	0.2131	7.2580E-04				
	d	0.1921	6.9951E-04				
3,2	a	0.2962	2.5598E-04	0.2877	8.847E-3	2.4723E-04	3.537E-05
	b	0.2806	2.1328E-04				
	c	0.2795	2.2660E-04				
	d	0.2944	2.9304E-04				
3,3	a	0.1968	2.5598E-04	0.1913	4.917E-3	6.8183E-05	6.8874E-06
	b	0.0664	8.7567E-05				
	c	0.1874	6.6353E-05				
	d	0.1896	7.5801E-05				
3,6	a	0.0576	1.8281E-05	0.0597	4.949E-3	1.7500E-05	7.6658E-07
	b	0.0538	1.6562E-05				
	c	0.0629	1.7218E-05				
	d	0.0646	1.7940E-05				
4,3	a	0.1705	5.4099E-05	0.1620	1.047E-2	5.3534E-05	4.9023E-06
	b	0.1602	5.0331E-05				
	c	0.1694	6.0240E-05				
	d	0.1479	4.9466E-05				
5,1	a	0.1175	8.7188E-04	0.1172	4.096E-3	8.7702E-04	1.1205E-05
	b	0.1216	8.6413E-04				
	c	0.1180	8.8931E-04				
	d	0.1117	8.8277E-04				
5,5	a	0.0629	1.6941E-05	0.0663	2.295E-3	1.5588E-05	1.4443E-06
	b	0.0680	1.5810E-05				
	c	0.0673	1.6053E-05				
	d	0.0669	1.3548E-05				

Appendix C Transient Response: Method of Multiple Time Scales

It is convenient to reorganize the equation of motion by introducing a bookkeeping parameter ε and collecting terms with the same order. The equation of motion can be cast as follows

$$\ddot{\chi} + \chi + \varepsilon \hat{k}_2 \chi^2 + \varepsilon^2 \left(\hat{k}_3 \chi^3 + \hat{c}_1 \dot{\chi} + \hat{c}_2 \dot{\chi} |\dot{\chi}| + \hat{c}_3 \dot{\chi}^3 \right) = 0. \tag{C.1}$$

Note that the equation above is equivalent to the equation in (7) except for the forcing component. In this case we considered the free response of the system subjected to initial conditions. The damping coefficients and the cubic stiffness are scaled at order ϵ^2 and the quadratic stiffness term is scaled on the order of ϵ. This implies that the following inequality must hold $\hat{k}_3 < \hat{k}_2 < \hat{k}_1 = 1$ for the asymptotic solution presented below to be valid.

The initial conditions can be written in their non-dimensional form as $\chi(0) = x(0)/L_c$ and $\dot{\chi}(0) = \dot{x}(0)/(L_c \omega_n)$. The time dependence is expanded into multiple scales $T_n = \epsilon^n \tau$, and the time derivatives can be written as

$$\frac{\partial}{\partial t} = D_0 + \varepsilon D_1 + \varepsilon^2 D_2 + \mathcal{O}(\varepsilon^3), \tag{C.2a}$$

$$\frac{\partial^2}{\partial t^2} = D_0^2 + 2\varepsilon D_0 D_1 + \varepsilon^2 \left(D_1^2 + 2 D_0 D_2 \right) + \mathcal{O}(\varepsilon^3), \tag{C.2b}$$

where $D_n = \partial / \partial T_n$. Furthermore, the time-dependent non-dimensional displacement χ can be expressed as

$$\chi(t; \varepsilon) = \sum_{i=0}^{2} \varepsilon^i \chi_i(T_0, T_1, T_2) + \mathcal{O}(\varepsilon^3). \tag{C.3}$$

Substituting Eqns.(C.2) and (C.3) in the Eqn.(C.1) and gathering terms with the same power of ε yields

$$\mathcal{O}(\varepsilon^0): \ D_0^2 \chi_0 + \chi_0 = 0, \tag{C.4a}$$

$$\mathcal{O}(\varepsilon^1): \ D_0^2 \chi_1 + \chi_1 = -2 D_0 D_1 \chi_0 - \hat{k}_2 \chi_0^2, \tag{C.4b}$$

$$\begin{aligned} \mathcal{O}(\varepsilon^2): \ D_0^2 \chi_2 + \chi_2 = & -2 D_0 D_1 \chi_1 - D_1^2 \chi_0 - 2 D_0 D_2 \chi_0 - 2 \hat{k}_2 \chi_0 \chi_1 - \hat{k}_3 \chi_0^3 - \hat{c}_1 D_0 \chi_0 - \hat{c}_3 (D_0 \chi_0)^3 + \\ & - \hat{c}_2 \left(g_1 \exp(i T_0) \mathrm{d} T_0 + \sum_{\substack{-\infty \\ n \neq 1}}^{\infty} g_n \exp(i n T_0) \right), \end{aligned} \tag{C.4c}$$

where g's are the Fourier's coefficients used to approximate the function $\dot{x}|\dot{x}|$, $g_n = g_n(A, \bar{A})$.

Solutions to the $\mathcal{O}(\varepsilon^0)$ expansion in Eqn. (C.4a) can be written as

$$\chi_0 = A(T_1, T_2) \exp\,(i T_0) + \bar{A}(T_1, T_2) \exp\,(-i T_0), \tag{C.5}$$

where $\bar{A}$ is the complex conjugate of A. Substituting into Eqn. (C.4b) yields

$$D_0^2 \chi_1 + \chi_1 = -2 i D_1 A \exp(i T_0) - \hat{k}_2 \left(A^2 \exp(2 i T_0) + A \bar{A} \right) + cc, \tag{C.6}$$

where cc denotes complex conjugate. To derive uniformly valid expansion, we must eliminate secular terms from the Eqn. (C.6) hence, $D_1 A = 0$; therefore, $A = A(T_2)$. The solution Eqn. (C.6) can be written as

$$\chi_1 = \hat{k}_2 \left(\frac{A^2}{3} \exp(2 i T_0) - A \bar{A} \right) + cc. \tag{C.7}$$

In view of the Eqns. (C.5) and (C.7), the $\mathcal{O}(\varepsilon^2)$ expansion in (C.4c) writes

$$\begin{aligned} D_0^2 \chi_2 + \chi_2 = & \left(2 i D_2 A + i \hat{c}_1 A + \frac{i \hat{c}_2 A^2}{2\pi} \int_0^{2\pi} \sin^2(\phi) \big| \sin(\phi) \big| \mathrm{d}\phi + 3 i \hat{c}_3 A^2 \bar{A} + 3 k_3 A^2 \bar{A} + \tfrac{10}{3} \hat{k}_2^2 A^2 \bar{A} \right) \exp(i T_0) \\ & - \left(2 \hat{k}_2^2 A^2 \left(\tfrac{A}{3} + 2 \bar{A} \right) - \hat{k}_3 A^3 - i \hat{c}_1 A^3 - i \hat{c}_3 A^3 \right) \exp(3 i T_0) - \hat{c}_2 \sum_{\substack{-\infty \\ n \neq 1}}^{\infty} g_n \exp(i n T_0). \end{aligned} \tag{C.8}$$

Secular terms can be eliminated from the expression of χ_2 if

$$i \left(2 D_2 A + \hat{c}_1 A + \frac{\hat{c}_2 A^2}{2\pi} \int_0^{2\pi} \sin^2(\phi) \big| \sin(\phi) \big| \mathrm{d}\phi + 3 \hat{c}_3 A^2 \bar{A} \right) + 3 k_3 A^2 \bar{A} + \tfrac{10}{3} \hat{k}_2^2 A^2 \bar{A} = 0, \tag{C.9}$$

where $\phi = T_0 + \beta$. It is then convenient to express A in polar form, i.e.

$$A = \tfrac{1}{2} a \exp\,(i\beta), \tag{C.10}$$

where a and β are real functions of the time scale T_2. By substituting Eqn.(C.10) into Eqn.(C.9) and separating the real and imaginary parts, the following set of equations is obtained.

$$\dot{a} = -\frac{\hat{c}_1}{2} a - \frac{4\hat{c}_2}{3\pi} a^2 - \frac{3\hat{c}_3}{8} a^3, \quad \text{and} \tag{C.11a}$$

$$a\dot{\beta} = \frac{10\hat{k}_2^2 - 9\hat{k}_3}{24} a^3. \tag{C.11b}$$

Finally, a_0 and β_0 are evaluated imposing the initial conditions as follows

$$a_0 \cos(\beta_0) = 0 \quad \text{and} \quad a_0 \sin(\beta_0) = -\dot{\chi}(0), \tag{C.12}$$

which yields

$$a_0 = -\dot{\chi}(0), \quad \text{and} \quad \beta_0 = \tfrac{\pi}{2} + 2m\pi, \quad \text{where } m \in \mathbb{Z}. \tag{C.13}$$

The modulation equations (C.11) were solved via numerical integration. Once the numerical solutions for the equations in (C.11) is obtained, the zeroth-order time response can be reconstituted as

$$\chi = a(\tau)\cos(\tau + \beta(\tau)). \tag{C.14}$$

In Figure 6, we compared the experimental time responses against the amplitude obtained with the method of multiple time scales.